Draft version January 29, 2026
Typeset using LaTeX **default** style in AASTeX7.0.1

Nucleus and Postperihelion Activity of Interstellar Object 3I/ATLAS Observed by Hubble Space Telescope

Man-To Hui (許文韜),[1] David Jewitt,[2] Max J. Mutchler,[3] Jessica Agarwal,[4] and Yoonyoung Kim (김윤영)[2]

[1] *Shanghai Astronomical Observatory, Chinese Academy of Sciences, No. 80 Rd Nandan, Shanghai 200030, Mainland China*
[2] *Department of Earth, Planetary, and Space Sciences, UCLA, 595 Charles Young Drive East, Los Angeles, CA 90095-1567, USA*
[3] *Space Telescope Science Institute, 3700 San Martin Drive, Baltimore, MD 21218, USA*
[4] *Institut für Geophysik und extraterrestrische Physik, Technische Universität Braunschweig, Mendelssohnstr. 3, 38106 Braunschweig, Germany*

(Received January 29, 2026; Revised 2026; Accepted DRAFT)

Submitted to ApJL

ABSTRACT

We report the successful detection of the nucleus of interstellar object 3I/ATLAS, achieved by applying the nucleus extraction technique to our Hubble Space Telescope (HST) observations from December 2025 to January 2026. The product of the V-band geometric albedo, p_V, with the physical cross-section of the nucleus is 0.22 ± 0.07 km^2, which corresponds to an effective radius of 1.3 ± 0.2 km if assuming $p_V = 0.04$, as is typical for cometary nuclei in the solar system. This size is in agreement with our estimate derived from the reported nongravitational effect and activity of the interstellar object. If the measured photometric variations are solely due to the rotation of an aspherical nucleus, the axis ratio must be 2 : 1 or greater, and the rotation period $\gtrsim 1$ hr. Leveraging the range of covered phase angles, we identified a significant opposition surge of ~ 0.2 mag with a width of $3^\circ \pm 1^\circ$, which may include concurrent contributions from orbital plane crossing and tail projection, and determined a linear phase slope of 0.026 ± 0.006 mag degree^{-1} for the coma dust. Compared to the preperihelion brightening trend, 3I faded more rapidly on the outbound leg, following an activity index of 4.5 ± 0.3, not unusual in the context of solar system comets. This activity asymmetry is further corroborated by a postperihelion coma surface brightness profile that is significantly shallower than its preperihelion counterpart. From the statistics, we infer that multiple interstellar objects resembling 3I likely went undetected even before the discovery of 1I/'Oumuamua.

Keywords: Comet nuclei (2160) — Comae (271) — Comets (280) — Interstellar objects (52)

1. INTRODUCTION

3I/ATLAS, formerly designated C/2025 N1 (ATLAS), was discovered by the Asteroid Terrestrial-impact Last Alert System (ATLAS) sky survey on 1 July 2025. Serendipitous prediscovery observations were quickly identified (e.g. A. D. Feinstein et al. 2025; J. Martinez-Palomera et al. 2025; Q. Ye et al. 2025), along with numerous followup observations, leading to the definitive identification of the object as the third interstellar object to intrude into our solar system (L. Denneau et al. 2025). Its trajectory is significantly more hyperbolic with respect to the Sun than those of the previous two interstellar objects, 1I/'Oumuamua and 2I/Borisov, with an eccentricity of $e = 6.14$. The closest approach of the object to the Sun occurred on 29 October 2025 at a perihelion distance of $q = 1.4$ au, implying an excess speed of ~ 58 km s^{-1}, which likely suggests a kinematic age of 3-11 Gyr for 3I, older than the previous interstellar objects (A. G. Taylor & D. Z. Seligman 2025). The object is statistically unlikely to have approached any star as closely as the current approach to the Sun (D. Jewitt & J. Luu 2025).

Numerous observations of 3I have been conducted using both ground-based facilities and spacecraft, spanning a wide range of wavelengths and utilising various techniques including imaging, spectroscopy, and polarimetry. In brief the interstellar object was reported to exhibit a steady growth of activity as it approached the Sun (e.g. M. R. Combi et al. 2025; D. Jewitt & J. Luu 2025; T. Santana-Ros et al. 2025), with peculiar dust scattering properties (Z. Gray et al. 2025; S. Choi et al. 2026), slightly enriched volatile content, and distinct outgassing behaviour (e.g. M. A. Cordiner et al. 2025; D. Hutsemékers et al. 2025; N. X.

Email: mthui@shao.ac.cn, manto@hawaii.edu

Table 1. Observing Geometry of 3I/ATLAS from HST

HST Observations				Observing Geometry							
Visit	Obs. Time & Date (UTC)[a]	t_{exp} (s)[b]	#[c]	r_H (au)[d]	Δ (au)[e]	α (°)[f]	ε (°)[g]	$\theta_{-\odot}$ (°)[h]	θ_{-V} (°)[i]	ψ (°)[j]	ν (°)[k]
1[†]	20:39-21:16 30 Nov 2025	260	6	1.798	1.913	30.6	68.2	293.7	109.9	2.4	44.4
2	21:22-21:52 12 Dec 2025	170	6	2.108	1.814	27.8	93.0	293.0	109.4	2.3	54.2
3	16:00-16:24 27 Dec 2025	170	5	2.536	1.830	18.3	126.0	291.4	107.0	1.9	62.7
4	15:32-16:08 07 Jan 2026	170	7	2.874	1.978	9.8	150.3	290.6	104.1	1.4	67.3
5	15:23-15:54 14 Jan 2026	170	6	3.095	2.135	4.8	164.7	293.1	102.0	1.0	69.7
6	13:12-13:42 22 Jan 2026	170	6	3.348	2.364	0.7	177.6	12.4→13.5	99.6	0.7	72.0

[a] Mid-exposure epoch of observation.

[b] Individual exposure time.

[c] Number of individual exposures.

[d] Heliocentric distance.

[e] HST-centric distance.

[f] Phase angle.

[g] Solar elongation.

[h] Position angle of antisolar direction projected in the sky plane of HST.

[i] Position angle of negative heliocentric velocity projected in the sky plane of HST.

[j] Orbital plane angle. Positive values indicate HST being above the orbital plane of 3I.

[k] True anomaly of the heliocentric orbit.

[†] Data not included for analysis due to the overexposure of 3I.

Roth et al. 2025). Its activity was dominated by CO_2 at heliocentric distances $r_H \gtrsim 3$ au, which was later overtaken by H_2O sublimation when closer to the Sun (e.g. M. R. Combi et al. 2025; M. A. Cordiner et al. 2025; Z. Xing et al. 2025; B. Yang et al. 2025). Conversely, there has been no successful observation of the nucleus of 3I to date, primarily because of hindrance by its activity, which began prior to the earliest available observations (e.g. Q. Ye et al. 2025). Our previous attempt to extract the nucleus signal of 3I from preperihelion Hubble Space Telescope (HST) observations in July 2025 yielded an upper limit of ~2.8 km for the nucleus radius (D. Jewitt et al. 2025). Nevertheless, characterising the radius of the nucleus is scientifically pivotal, as an essential input for physical models and a constraint on the population of interstellar objects as a whole. In this letter, we report the first successful detection of the nucleus of 3I using postperihelion optical imaging from our HST program.

2. OBSERVATIONS

Our postperihelion observations of interstellar object 3I were conducted using the 2.4 m HST and the UVIS channel of the Wide Field Camera 3 (WFC3) camera. Data were acquired through the broadband F350LP filter from late 2025 to early 2026 under the Director's Discretionary (DD) program 18152. The filter, characterised by a central wavelength of 5846 Å and a full-width-half maximum (FWHM) of 4758 Å, enabled us to fully leverage the maximal sensitivity of the facility. To reduce overheads we used only the 2047 × 2050 full quadrant UVIS2-2K2C-SUB aperture for readout, which provides a nearly square field of view of ~81″ × 81″ at a pixel scale of 0.″04 pixel^{-1}. During each HST visit, we collected multiple consecutive exposures tracking the ephemeris position of 3I. The observation configurations and corresponding observing geometries of 3I are summarised in Table 1.

3. NUCLEUS SIZE ANALYSIS

The charge transfer efficiency (CTE) of the UVIS channel degrades over time, and therefore, appropriate corrections are necessary to mitigate signal losses (see the Wide Field Camera 3 Instrument Handbook). We started with the calibrated, flat-

fielded, and CTE-corrected HST data from our program, retrieved from the Barbara A. Mikulski Archive for Space Telescopes (MAST) site. Cosmic rays were eliminated using the Laplacian cosmic-ray rejection algorithm `L.A.Cosmic` (P. G. van Dokkum 2001) for the Image Reduction and Analysis Facility (`IRAF`; D. Tody 1986).[5] Regions free of cosmic-ray contamination remained untouched by this process, with the only exception that overexposed star trails were mistakenly modified by `L.A.Cosmic`. This had no impact on our result, however, as none of these trails were in the vicinity of the photocenter of the interstellar object.

Prior to performing photometry, we utilised the WFC3 UVIS Imaging Exposure Time Calculator and the stellar spectral flux library by A. J. Pickles (1998) covering possible spectral slopes of long-period comets in the solar system (e.g. D. Jewitt 2015) to simulate the image zero-point for objects of similar colours. The resulting scatter was treated as the uncertainty associated with the image zero-point.

3.1. *Conservative Constraint*

The bright and centrally condensed coma of 3I precluded direct measurement of the nucleus. We therefore attempted to isolate and remove the coma contribution to the photometry of the nucleus in different ways. The simplest method is to treat the coma contiguous to the photocentric region as the foreground (background in photometry), which inevitably underestimates the contribution of the coma in the near-nucleus region, thereby yielding an upper limit for the nucleus signal.

We measured the total flux within a circular aperture 0.″16 (4 pixels) in radius at the photocenter of 3I, from which we subtracted the background flux within a contiguous annulus extending to 0.″24 (6 pixels) from the photocenter. These flux measurements were then converted to apparent magnitudes using the simulated image zero-point.

The apparent magnitudes are functions of heliocentric distance ($r_{\rm H}$), HST-centric distances (Δ), and phase angle (α), all of which evolved over the course of our HST observations. We normalised both distances to $r_\oplus = 1$ au and corrected for phase effects by assuming a linear phase model with a slope of $\beta_\alpha = 0.04 \pm 0.02$ mag deg^{-1} (e.g. P. L. Lamy et al. 2004; M. M. Knight et al. 2024) to compute the absolute magnitude:

$$H_{{\rm n},V} = m_{{\rm n},V} - 5\log\left(r_{\rm H}\Delta\right) - \beta_\alpha\alpha, \tag{1}$$

where $m_{{\rm n},V}$ is the apparent magnitude of the nucleus, $r_{\rm H}$ and Δ are expressed in au, and α is phase angle in degrees. We thereby determined a lower bound of $H_{{\rm n},V} \gtrsim 15$ across the five HST epochs for the nucleus of the interstellar object, consistent with $H_{{\rm n},V} \gtrsim 15.4$ from the preperihelion HST measurement (D. Jewitt et al. 2025).

Reformulated from D. Jewitt (1991), the optical cross-section of the nucleus at zero phase angle, denoted $C_{\rm n}$, is related to the absolute magnitude by the following equation:

$$\begin{aligned} C_{\rm n} &\triangleq p_V \Xi_{\rm n} \\ &= 10^{0.4\left(m_{\odot,V} - H_{{\rm n},V}\right)} \pi r_\oplus^2, \end{aligned} \tag{2}$$

where p_V is the V-band geometric albedo, $\Xi_{\rm n}$ is the effective geometric cross-section ($\Xi_{\rm n} = \pi R_{\rm n}^2$ for a spherical nucleus of radius $R_{\rm n}$) of the nucleus, and $m_{\odot,V} = -26.76 \pm 0.03$ is the apparent V-band magnitude of the Sun as observed at a heliocentric distance of $r_\oplus = 1$ au (C. N. A. Willmer 2018). Substitution yields $C_{\rm n} \lesssim 2$ km^2 for all HST epochs. Assuming a spherical shape and a nominal value of $p_V = 0.04$ typical for cometary nuclei (e.g. P. L. Lamy et al. 2004; M. M. Knight et al. 2024), but as yet unconstrained for 3I, we derived a conservative upper limit estimate for the nucleus radius of 3I of $R_{\rm n} \lesssim 4$ km.

3.2. *Nucleus Extraction*

We next applied a nucleus extraction technique originally devised by P. L. Lamy & I. Toth (1995) and implemented by P. L. Lamy et al. (1998). By employing this technique, we successfully detected the nucleus of long-period comet C/2014 UN$_{271}$ (Bernardinelli-Bernstein) from our HST program using similar observing configurations (M.-T. Hui et al. 2022). Basically, the technique assumes an optically thin coma and decomposes the total surface brightness into distinct contributions from the nucleus and coma as

$$\Sigma\left(\rho,\theta\right) = k_{\rm n}\mathcal{P}\left(\rho,\theta\right) + \left[k_{\rm c}\left(\theta\right)\left(\frac{\rho}{\rho_0}\right)^{-\gamma(\theta)}\right] * \mathcal{P}\left(\rho,\theta\right), \tag{3}$$

where the total surface brightness is a function of both the projected distance from the photocenter, ρ, and the azimuthal angle, θ. The first term on the right-hand side of Equation (3) represents the nucleus signal, modelled as the volume-normalised point-spread function (PSF, denoted $\mathcal{P}$) of the WFC3 camera using the `TinyTim` package (J. E. Krist et al. 2011) and scaled by a

[5] The code is publicly available at the L.A.Cosmic website.

constant factor k_n. The second term represents the contribution from the coma, approximated by an azimuth-dependent power-law model. The nucleus + coma model is convolved with the instrument PSF, with the symbol $*$ denoting the convolution operator. The pre-convolution surface brightness profile of the coma is parametrised by scaling factor k_c and logarithmic surface brightness gradient γ, both as functions of the azimuthal angle. A spherically symmetric coma in steady state has $\gamma = 1$, whereas solar radiation pressure steepens the gradient to $\gamma = 1.5$ in the sunward direction (D. C. Jewitt & K. J. Meech 1987). We adopted a normalisation distance of $\rho_0 = 1$ pixel to ensure that both scaling factors share the same units.

Following M.-T. Hui & J.-Y. Li (2018) we assigned a weighting map based on Poisson statistics to each individual exposure and utilised the Levenberg-Marquardt algorithm via `MPFIT` (C. B. Markwardt 2009) to determine the best-fit surface brightness profiles for the coma. The fits were restricted to an annular region between 0.″24 and 1.″20 in radius from the photocenter of 3I. The results are shown as functions of azimuth in Figure 1, where sharp fluctuations are caused by residual cosmic-ray artifacts. We performed azimuthal median smoothing to these fits (shown as solid curves in Figure 1) and applied the resulting parameters to reconstruct the surface brightness profile of the coma on a sevenfold-subsampled grid, including the near-nucleus region, which is interior to the fitted annulus. After subtracting the coma model from each exposure and resampling the resulting image back to the original pixel scale, a distinct positive residual feature was revealed at the original photocentric position. The FWHM of this feature is statistically consistent with the WFC3 PSF model generated by `TinyTim`, although faint jet-like features remain. Consequently, we interpret this residual as the detected nucleus of 3I. Figure 2 displays the observed, modelled, and residual images of the interstellar object for each HST visit.

We next performed PSF photometry on the residual signal with `psffit` from Buie's IDL library. Results for each HST visit are listed in Table 2, while comparisons of the observed and modelled radial brightness profiles and the apparent magnitude time series are shown in Figures 3 and 4, respectively. We were fully aware that the extracted nucleus flux possibly fell inside the caution zone where results can be biased by the nucleus extraction technique (M.-T. Hui & J.-Y. Li 2018). To investigate the reliability of the results, we varied the azimuthal smoothing window width, image subsampling factor, and the fitted annular region within the ranges suggested by M.-T. Hui & J.-Y. Li (2018), and we even switched to aperture photometry on the residual feature using an aperture radius corresponding to its FWHM so as to better exclude jet-like features in the near-nucleus region. We found the results to be consistent within the noise level regardless of the parameter choices. Furthermore, applying the method described in Section 3.1 to the whole image sequence yielded the same temporal trends as those shown in Figure 4, albeit with a systematic brightness offset due to contamination from the coma. Therefore, we conclude that the nucleus extraction technique successfully revealed the nucleus of 3I. Our previous attempt using preperihelion HST observations (D. Jewitt et al. 2025) was likely unsuccessful both as a result of lower spatial resolution at a greater (3.0 au) geocentric distance and a steeper preperihelion radial brightness profile of the coma.

Figure 4 shows tentative evidence for brightness variations, consistent with the rotation of an aspherical nucleus and/or with activity fluctuations in the near-nucleus coma. Unfortunately, our data are too sparsely sampled to permit any useful estimate of the nucleus rotation period, except that it is likely $\gtrsim 1$ hour. If rotation is the pure cause of the brightness variations we use the observed magnitude range, $\gtrsim 0.8$ mag, to estimate the nucleus axis ratio projected into the plane of the sky of $\gtrsim 2:1$. However, this axis ratio could be lower, and even potentially all the way down to unity, if a significant portion of the variability stems from dust activity. Averaging these measurements yields a nucleus radius $R_n = 1.3 \pm 0.2$ km for 3I, much larger than the nuclei of 1I/'Oumuamua (highly aspherical, but effective radius ~ 0.08 km) and 2I/Borisov (~ 0.4 km) (D. Jewitt & D. Z. Seligman 2023, and citations therein).

4. DISCUSSIONS

4.1. *Nucleus Size Inferred from Nongravitational Effect*

The nongravitational effect of 3I allowed us to estimate its nucleus size from an independent approach, which in turn can be compared with the results derived from our HST observations. The orbital solution of 3I by JPL Horizons demonstrates a statistically significant detection of a nongravitational effect, presumably due to anisotropic mass loss from the object. Using an inverse square law for the nongravitational force model, i.e. $g_{NG} \propto r_H^{-2}$, the solution yields the radial, transverse, and normal (RTN) components of the nongravitational parameters, originally defined by B. G. Marsden et al. (1973), to be $A_1 = (+4.5 \pm 0.1) \times 10^{-8}$ au day^{-2}, $A_2 = (+1.7 \pm 0.1) \times 10^{-8}$ au day^{-2}, and $A_3 = (-6.0 \pm 0.3) \times 10^{-9}$ au day^{-2}, respectively.[6] Based on the law of conservation of momentum and assuming a spherical nucleus, the nucleus radius can be inferred from the nongravitational effect

[6] Retrieved on 26 January 2026.

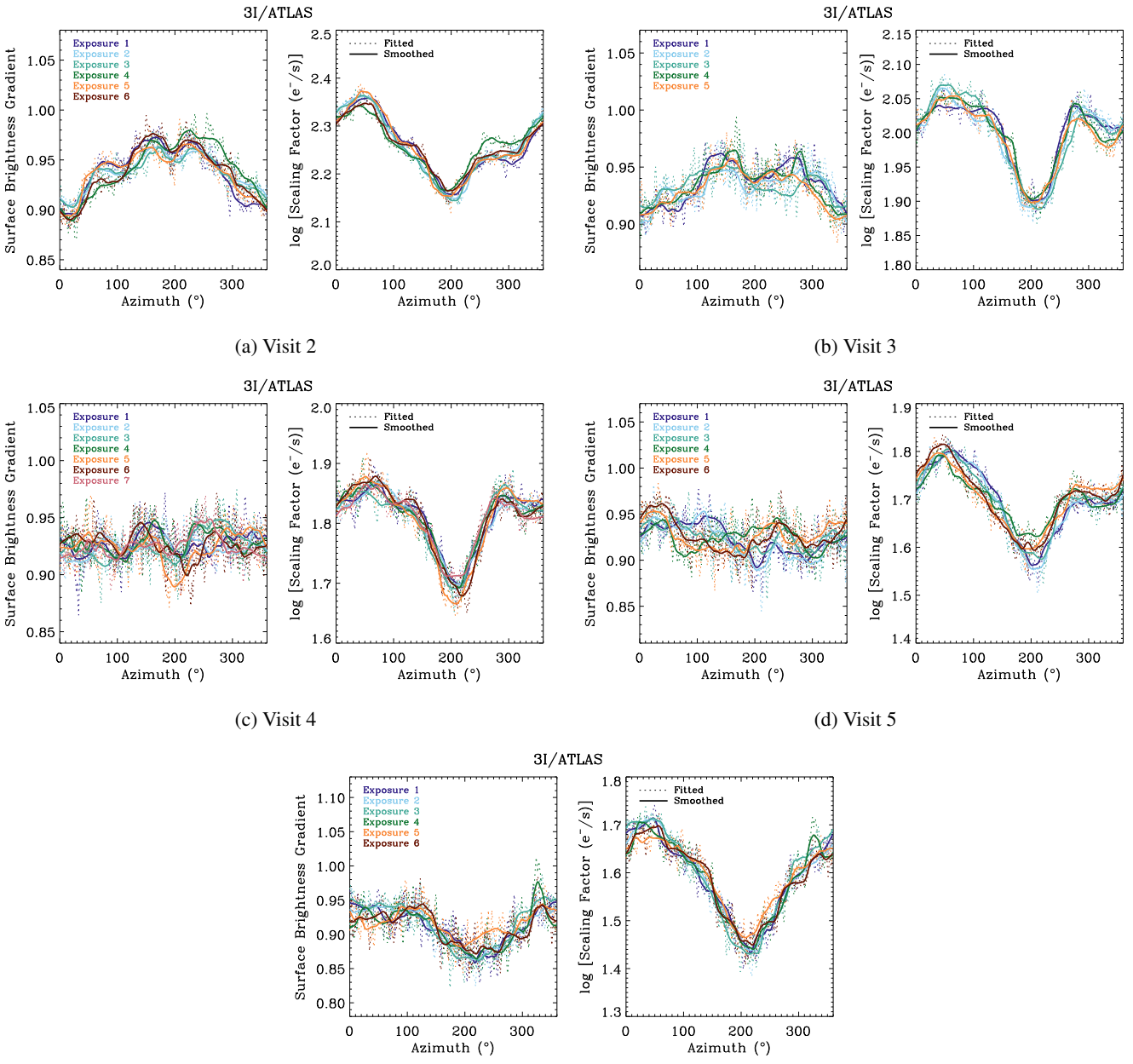

(a) Visit 2

(b) Visit 3

(c) Visit 4

(d) Visit 5

(e) Visit 6

Figure 1. Best-fit parameters for the surface brightness profile of the coma as functions of azimuth (measured from J2000 celestial equatorial north in an anticlockwise direction). The fits were performed within an annular region between 6 pixels (0.″24) and 30 pixels (1.″20) from the photocenter of 3I/ATLAS. Panels represent results from (a) Visit 2 on 12 December 2025, (b) Visit 3 on 27 December 2025, (c) Visit 4 on 7 January 2026, (d) Visit 5 on 14 January 2026, and (e) Visit 6 on 21 January 2026. Data from individual exposures are color coded. Solid lines represent the results of a median smoothing applied to the best fits with an azimuthal window of 30°.

and the outgassing mass loss using the formulation by M.-T. Hui et al. (2020):

$$R_{\rm n} = \left[\frac{3\kappa \mathscr{U}_{\rm gas} \mathfrak{m}_{\rm u}}{4\pi\rho_{\rm n} \sqrt{\sum_{j=1}^{3} A_j^2}} \left(\frac{Q_{\rm gas} v_{\rm gas}}{g_{\rm NG}} \right) \right]^{1/3} . \tag{4}$$

Here κ is the collimation coefficient of activity, with a lower bound of 0 indicating an isotropic scenario and an upper bound of 1 corresponding to perfectly collimated outgassing, $\mathscr{U}_{\rm gas}$ is the relative molecular mass of the dominant outgassing substance,

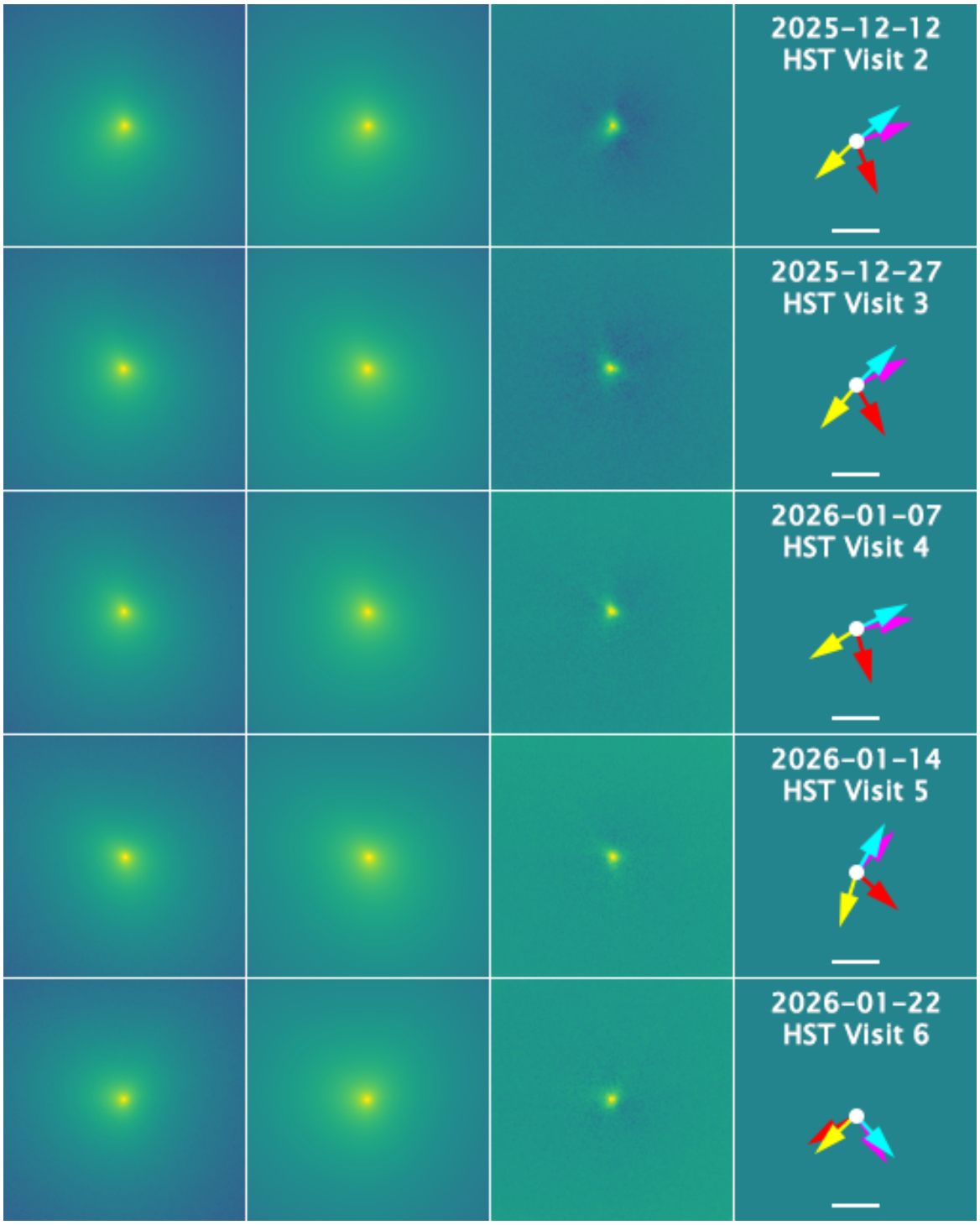

Figure 2. Detection of the nucleus of 3I (third panel from the left) via subtraction of the best-fit coma model (second panel) from the observed HST images (first panel) for each HST visit (indicated at right). For illustrative purposes, the shown images are median-combined from individual exposures within each visit and displayed with a logarithmic intensity stretch. In each row, the red and magenta arrows indicate local north and east, respectively, in the J2000 equatorial coordinate system, with the projected antisolar direction and the negative heliocentric velocity of 3I represented by the yellow and cyan arrows, respectively. The horizontal white bar near the bottom marks a scale of 1″ in apparent length.

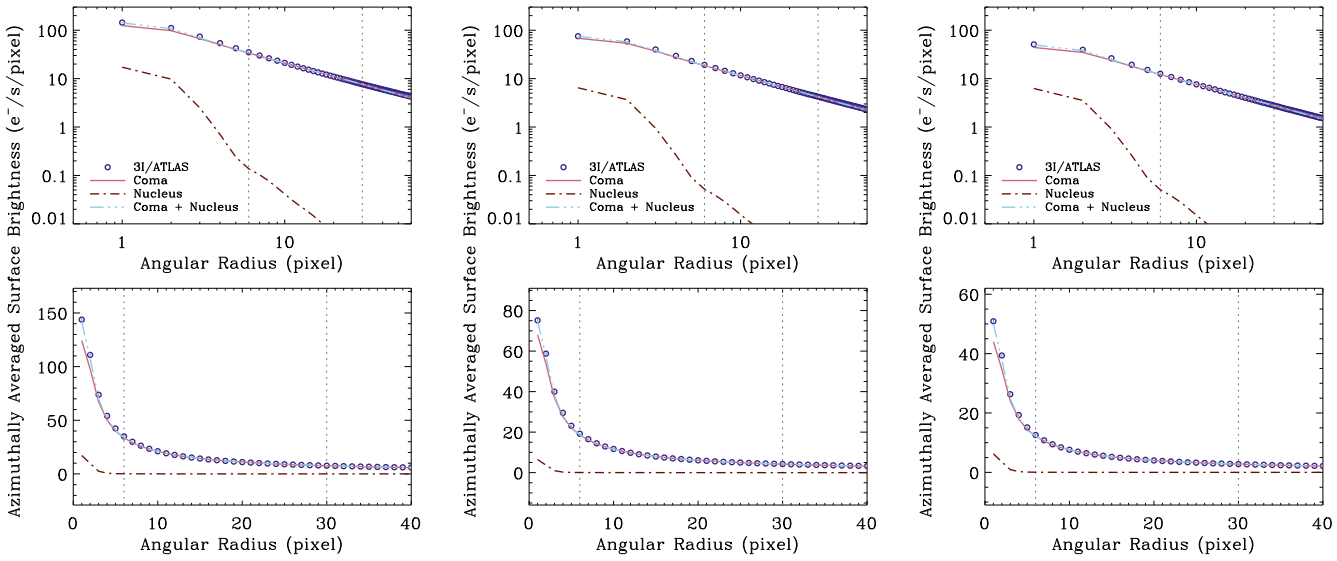

(a) Visit 2 (b) Visit 3 (c) Visit 4

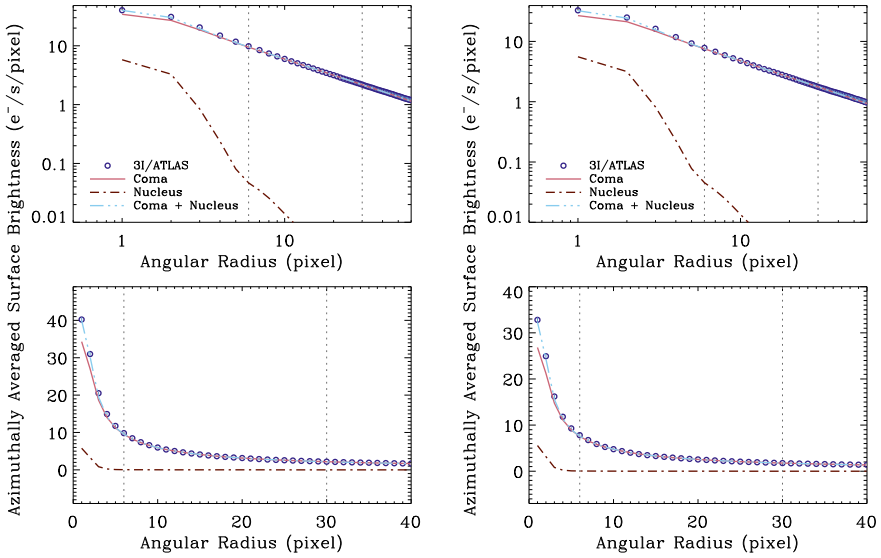

(d) Visit 5 (e) Visit 6

Figure 3. Comparison between the observed radial surface brightness profile (dark red diamonds) and the best-fit model (light blue dashed-dotted line) for the first exposure of 3I/ATLAS from (a) Visits 2 on 12 December 2025, (b) Visit 3 on 27 December 2025, (c) Visit 4 on 7 January 2026, (d) Visit 5 on 14 January 2026, and (e) Visit 6 on 21 January 2026. The best-fit coma and nucleus components are shown as pink solid and dark red dashed-dotted curves, respectively. Formal 1σ uncertainties are plotted as well but are largely obscured by the markers at the displayed scales. In each panel, the top and bottom sub-panels display the same data on log-log and linear scales, respectively. Grey vertical dotted lines mark the inner and outer boundaries (6 and 30 pixels, or 0.″24 and 1.″20, respectively) of the annular region used for fitting the coma. Results for the subsequent exposures are visually consistent and are therefore omitted for clarity.

$\mathfrak{m}_u = 1.66 \times 10^{-27}$ kg is the atomic mass constant, $\rho_n = 0.5$ g cm^{-3} is the assumed bulk density of the nucleus (O. Groussin et al. 2019, and citations therein), Q_{gas} and v_{gas} are, respectively, the molecular production rate and the outflow speed of the dominant outgassing substance. The three terms inside the parentheses in Equation (4) are functions of heliocentric distance, while the others are constants or treated as such for simplicity.

We evaluated the nongravitational effect of 3I around the time of perihelion when its outgassing activity and the resulting nongravitational acceleration were most pronounced. At $r_H = 1.401$ au, the interstellar object exhibited significant water production

Table 2. Photometry and Physical Properties of 3I/ATLAS Nucleus

Visit	Apparent Magnitude	Absolute Magnitude	Optical Cross-section	Radius[c]
	m_V	H_V	C_n (km^2)	R_n (km)
2	20.56 ± 0.03 (0.12)	16.54 ± 0.23 (0.12)	0.33 ± 0.07 (0.04)	1.63 ± 0.17 (0.09)
3	21.12 ± 0.05 (0.18)	17.06 ± 0.17 (0.20)	0.20 ± 0.03 (0.04)	1.28 ± 0.10 (0.12)
4	21.24 ± 0.05 (0.10)	17.07 ± 0.09 (0.11)	0.20 ± 0.02 (0.02)	1.28 ± 0.05 (0.06)
5	21.58 ± 0.07 (0.15)	17.29 ± 0.08 (0.15)	0.16 ± 0.01 (0.02)	1.15 ± 0.04 (0.08)
6	21.84 ± 0.09 (0.24)	17.32 ± 0.09 (0.24)	0.15 ± 0.01 (0.04)	1.12 ± 0.05 (0.13)
Summary				
mean (median) ± standard deviation	17.08 (17.07) ± 0.35	0.22 (0.21) ± 0.07	1.29 (1.28) ± 0.21	

NOTE—All magnitudes are reported in the V band. We assumed a nominal geometric albedo of $p_V = 0.04$ to derive the nucleus radii. For each visit, we provide both the standard error of the weighted mean and the standard deviations, with the latter in parentheses. For the summary line, the format is stated explicitly therein. We applied equal weighting so as to better prevent the mean from being skewed by measurements taken at smaller phase angles.

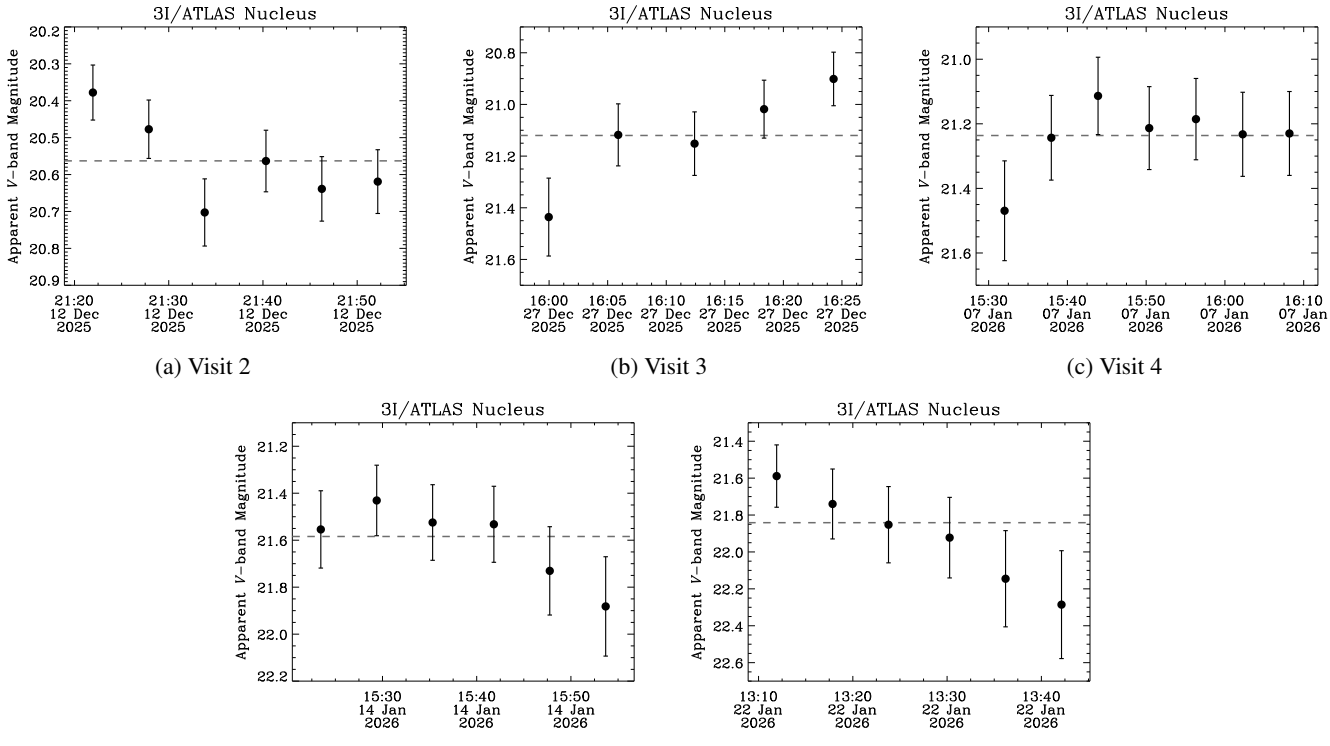

(a) Visit 2 (b) Visit 3 (c) Visit 4

(d) Visit 5 (e) Visit 6

Figure 4. Temporal apparent magnitude variations of the nucleus of 3I across the HST visits. The horizontal dashed line in each panel marks the mean value computed from the respective visit.

at a rate of $Q_{gas} = (3.2 \pm 1.0) \times 10^{29}$ s^{-1}, which subsequently declined during the outbound leg (M. R. Combi et al. 2025). [7]

[7] At the time of writing, H. Tan et al. (2026) reported water production rates up to an order of magnitude lower than M. R. Combi et al. (2025), despite using the same dataset. While this difference deserves to be investigated, applying the correlation from L. Jorda et al. (2008) to the near-perihelion magnitudes of 3I reported by Q. Zhang & K. Battams (2025) yielded water production rates of 3I in good agreement with M. R. Combi et al. (2025) at similar heliocentric distances, albeit preperihelion, and so we do not adopt the results of H. Tan et al. (2026).

Table 3. Comparisons of Nucleus Size Estimates of 3I/ATLAS

Nucleus Radius (km)	Source	Method
0.26-0.37	T. M. Eubanks et al. (2025)	Nongravitational effect
0.41-0.53	J. C. Forbes & H. Butler (2025)	Nongravitational effect
1.3 ± 0.2	This work	Nucleus extraction
$1.5 \pm 0.1^{\dagger}$	This work	Nongravitational effect
< 2.8	D. Jewitt et al. (2025)	Nucleus extraction
> 2.5	R. Cloete et al. (2025)	Nongravitational effect
$\leq 6.3 \pm 0.8^{\ddagger}$	C. O. Chandler et al. (2025)	Surface profile comparison
$< 11 \pm 1^{\ddagger}$	D. Z. Seligman et al. (2025)	Aperture photometry

† The collimation coefficient of activity was assumed to be $\kappa = 0.5$. For alternative values of $\kappa \in (0, 1)$, the size estimate scales as $\propto \kappa^{1/3}$ per Equation (4).

‡ To ensure consistency, estimates originally derived by other authors assuming $p_V = 0.05$ have been rescaled to match our adopted value of $p_V = 0.04$.

Setting $\mathscr{U}_{\rm gas} = 18$ for water, $\kappa = 0.5$ to approximate hemispherical emission, and adopting the empirical law for outflow speed of gas from A. L. Cochran & D. G. Schleicher (1993) yielding $v_{\rm gas} \approx 0.7$ km s^{-1}, we obtained the nucleus radius of 3I from Equation (4) to be 1.5 ± 0.1 km, in excellent agreement with our results in Section 3.2 via the nucleus extraction technique, thereby solidifying our nucleus size estimate.

Here the formal uncertainty was properly propagated from the covariance matrix of the RTN nongravitational parameters provided by Horizons and the reported error in the water production rate in M. R. Combi et al. (2025). However, we emphasise that this uncertainty is likely a significant underestimate, as it does not account for the systematic uncertainty in the unknown activity collimation coefficient. The maximum nucleus size permitted by the detected nongravitational acceleration occurs under a fully collimated mass-loss scenario, i.e. $\kappa = 1$, which yields $R_{\rm n} \leq 1.9 \pm 0.2$ km. Furthermore, this size estimate should also be considered as an upper limit to the radius if it should be the case that a significant part of the measured water production is due to the sublimation of icy grains in the coma.

Our inferred nucleus size estimate is notably much larger than earlier results by T. M. Eubanks et al. (2025) and J. C. Forbes & H. Butler (2025), despite using the same methodology. We posit that earlier solutions of the nongravitational parameters were less reliable due to the shorter observed arc, where potential biases, such as tailward offsets in astrometric measurements, could be more easily absorbed into the orbital fits. Furthermore, the applied nongravitational force model might have been overly simplified and therefore failed to closely approximate earlier epochs when outgassing of 3I was still weak and the nongravitational effect was far less insignificant.

In Table 3, we compare our nucleus size estimates of 3I with earlier results. Although the nucleus extraction technique yielded results falling within the caution zone, we remain confident that our nucleus size estimate through this technique is trustworthy because of the consistency between these two independent methods.

4.2. *Statistics of Similar Interstellar Interlopers*

We attempted to evaluate the statistics of interstellar interlopers similar in size to 3I inside our solar system. Based on 1I/'Oumuamua alone, D. Jewitt et al. (2017) and A. Do et al. (2018) derived a number density for such objects of $\sim$ 0.1-0.2 au^{-3} in the solar system. The subsequent discovery of the larger object 2I/Borisov was not a fluke but was in line with the extrapolated statistics (D. Jewitt et al. 2020). Recently, D. Z. Seligman et al. (2025) reported a number density of $\sim 3 \times 10^{-4}$ au^{-3} for 3I-like objects with $H_V = 12.5$. However, since this absolute magnitude overestimated the nucleus size due to contamination from the coma, the real number density was underestimated. From Figure 8 in D. Z. Seligman et al. (2025), we estimated an updated number density of $\sim 3 \times 10^{-3}$ au^{-3} for 3I-sized interstellar objects as detected by the ATLAS survey. Given the discovery of 3I at a heliocentric distance of $r_{\rm H} \approx 4.5$ au, this implies a total number of ~ 1 similar interstellar object within a sphere of this radius at the Sun at any instant on average. Therefore, the discovery of 3I is not unexpected.

If extrapolated from the statistics solely based on 1I/'Oumuamua using a differential size distribution index of -3, the total number of 3I-sized or larger interstellar objects inside the same volume of space around the Sun will be $\sim$0.2-0.3. The likelihood

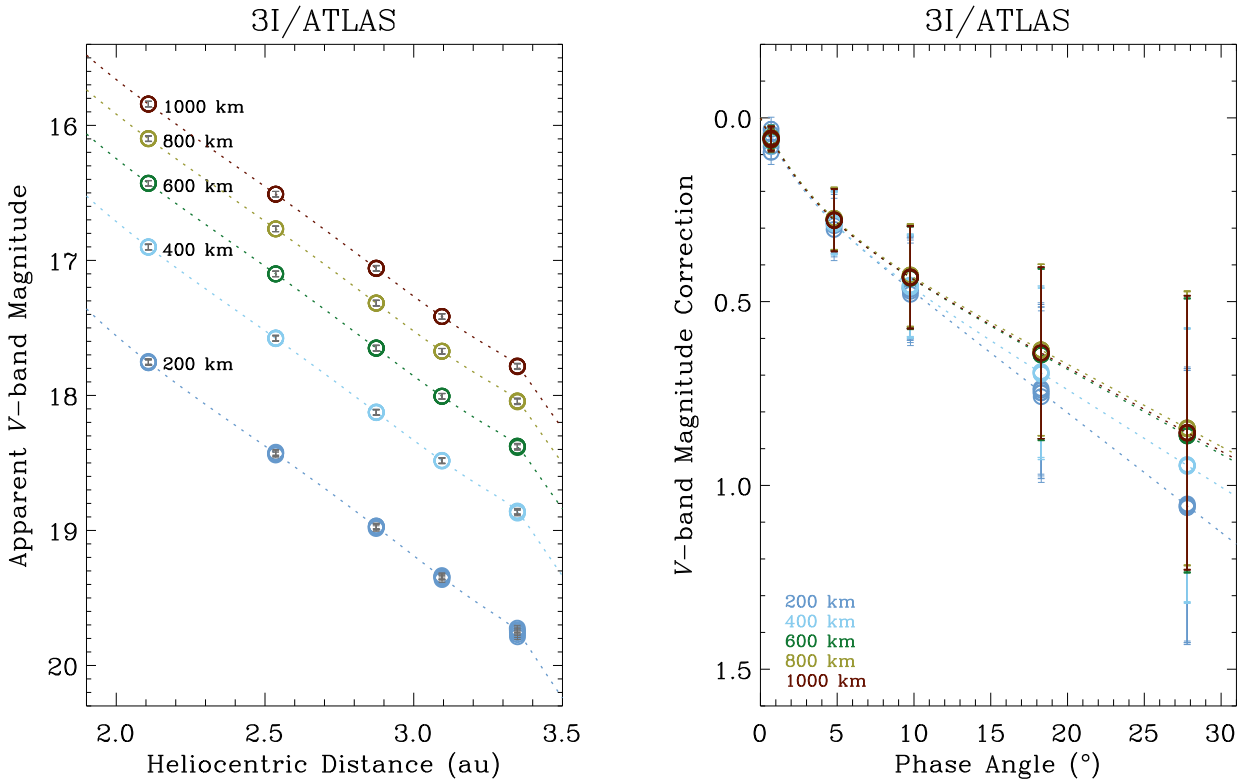

(a) (b)

Figure 5. Left: Apparent V-band magnitude of postperihelion 3I/ATLAS as a function of heliocentric distance across different apertures of fixed linear radii (colour coded and labelled). Right: V-band magnitude correction versus phase angle, highlighting the opposition effect. Best-fit models incorporating the linear-exponential phase function are drawn as dotted curves.

of detecting such an object is given by Poisson statistics to be ∼0.2-0.5, which drops to ∼(1−2) % for a steeper size distribution of -4. However, these likelihood estimates should only be treated as lower limits because cometary activity undoubtedly enhances the detectability of 3I-like objects. We conclude that the discovery of 3I remains in qualitative agreement with the previous statistics of the interstellar object population. The arrival rate of 3I-like interstellar objects, estimated from the ratio of their total number within the 4.5 au radius sphere to the corresponding crossing timescale, $\sim 2 \times 10^7$ s, is ∼1 per year.

Although all-sky surveys such as Pan-STARRS and Catalina have been operational for over a decade, only two other interstellar objects were previously discovered, both of which were visually fainter than 3I. Around its peak brightness, 3I was sufficiently bright that even visual comet hunters could have detected it had it passed through the inner solar system prior to the era of automated sky surveys. Here we simplistically estimated the likelihood that no 3I-like interstellar objects passed by between mid-1990s, the advent of modern sky surveys, and the discovery of 1I/'Oumuamua in 2017. Using Poisson statistics for this ∼ 20-year interval, we found the probability of no detectable 3I-like objects to be ∼ 10^{-13}, which is unrealistically minuscule. While earlier surveys were undeniably less sensitive if compared to contemporaneous ones, it seems unlikely that they were less efficient by many orders of magnitude. Therefore, it appears highly probable that several 3I-like interstellar objects passed through the inner solar system undetected between the advent of automated sky surveys and the discovery of 1I/'Oumuamua.

4.3. *Dust Activity & Scattering Phase Function*

Aside from characterising the nucleus of 3I, we analysed its postperihelion activity and the scattering properties of its dust grains using HST observations covering a month-long baseline and a wide range of phase angles (see Table 1). Similar to the photometric procedure in Section 3.1, we performed aperture photometry at the photocenter of the interstellar interloper but employed multiple apertures with constant linear radii at the projected HST-centric distance of 3I so as to sample the same cross-section regardless of varying distances. We used fixed linear radii from 200 km to 1000 km in 200 km increments. The sky background was measured from a concentric annular region with radii extending from ∼ 32″ to 79″ (800-2000 pixels) to

Table 4. Best-Fit Postperihelion Lightcurve Models of 3I/ATLAS

Aperture Radius (km)	Absolute Magnitude $H_{c,V}$	Activity Index n	Linear Phase Slope β_α (mag deg^{-1})	Opposition Effect Magnitude m_{OE}	Opposition Effect Width w_{OE} (°)	Normalised Residual RMS[†]
200	11.5 ± 0.7	4.8 ± 0.6	0.03 ± 0.01	0.15 ± 0.02	2 ± 2	0.551
400	11.0 ± 0.9	4.5 ± 0.7	0.03 ± 0.01	0.21 ± 0.03	3 ± 2	0.137
600	10.8 ± 1.0	4.3 ± 0.7	0.02 ± 0.01	0.22 ± 0.03	4 ± 2	0.087
800	10.5 ± 1.0	4.3 ± 0.7	0.02 ± 0.01	0.23 ± 0.03	4 ± 2	0.060
1000	10.2 ± 0.9	4.3 ± 0.7	0.02 ± 0.01	0.23 ± 0.03	3 ± 2	0.048
Mean	–	4.5 ± 0.3 (0.2)	0.026 ± 0.006 (0.005)	0.19 ± 0.01 (0.04)	3 ± 1 (1)	–

[†] Root mean square of the observed-minus-calculated residual sigma.

NOTE—The presented mean values are weighted means computed from measurements across all apertures, followed by their associated standard errors and standard deviations listed in parentheses.

minimise contamination from the dust environment of 3I. Using annuli further from the photocenter did not materially alter the results but instead increased uncertainty because reduced area within the FOV of the WFC3 camera fell inside the annuli.

We modelled the apparent magnitude of 3I as a function of heliocentric distance, HST-centric distance, and phase angle, following the formalism of Equation (1):

$$m_{c,V} = H_{c,V} + 2.5n \log r_H + 5 \log \Delta + \beta_\alpha \alpha, \tag{5}$$

in which $H_{c,V}$ is technically the heliocentric magnitude of 3I at $r_H = 1$ au but is still termed absolute magnitude here, and n is the activity index parametrising the heliocentric dependency of activity, with $n = 2$ corresponding to a constant effective cross-section. These two parameters, along with the linear phase slope β_α, which was held fixed for the nucleus in Section 3, were treated as free parameters of the model. Utilising the Levenberg-Marquardt approach in `MPFIT`, we obtained best-fit parameters and their uncertainties derived from the 3×3 covariance matrix, properly propagated from the individual measurement errors. The best fits yielded weighted mean values $\bar{n} = 4.7 \pm 0.2$ and $\bar{\beta}_\alpha = 0.035 \pm 0.003$ mag deg^{-1} for the activity index and linear phase slope, where the uncertainties represent standard errors, as the values remained statistically consistent across aperture sizes. However, the best fits all yielded reduced χ^2 values $\chi^2_\nu > 2$, implying residuals significantly greater than the measurement uncertainties. By examining the resulting magnitude correction with respect to the absolute magnitude as a function of phase angle (hereafter phase function for conciseness, and denoted ϕ), we clearly detected what appears to be an opposition surge in 3I, deviating from the trend predicted by the purely linear phase function.

Therefore, we refitted the apparent magnitude of 3I by replacing the fourth term in Equation (5) with the modified linear-exponential phase function from V. Rosenbush et al. (2002):

$$\phi(\alpha) = \beta_\alpha \alpha + m_{OE} \left[1 - \exp\left(-\frac{\alpha}{w_{OE}} \right) \right], \tag{6}$$

where β_α is the slope of the linear portion of the phase function, m_{OE} is the opposition surge in magnitude, and and w_{OE} characterises the e-folding width of the opposition effect. The inclusion of these two additional free parameters considerably improved the reduced χ^2 values by at least an order of magnitude, and by up to a factor of $\sim 10^3$ for several apertures. We compare our measurements against the best-fit models in Figure 5) and tabulate the best-fit parameters in Table 4), where mean values except for the absolute magnitude along with the respective standard errors and standard deviations are also appended, in that the best-fit absolute magnitude of 3I brightens with growing aperture size as expected as a consequence of more effective cross-section of dust grains in the coma being measured, while the other best-fit parameters remain consistent across different apertures.

Preperihelion continuum photometry from $r_H = 4.6$ au to 1.8 au revealed a steady brightening of 3I well described by an activity index $n = 3.8 \pm 0.3$ (D. Jewitt & J. Luu 2025). Our results show that over similar ranges of heliocentric distance, 3I faded more rapidly on the outbound leg than it brightened on the inbound leg.[8] This activity asymmetry is further corroborated by the fact that the coma of 3I exhibited a significantly steeper surface brightness gradient preperihelion ($\gamma > 1$; D. Jewitt et al. 2025; D. Jewitt & J. Luu 2025) than the shallower postperihelion profile with $\gamma < 1$ found in Section 3.2 (see Figure 1). The heliocentric index is influenced by many unmeasured parameters of the nucleus, among them the distribution of surface volatiles and the direction of the nucleus spin vector. It is thus impossible to ascribe a unique interpretation to the measured change. We note, however, that measurements of solar system comets show that the heliocentric index can decrease or increase after perihelion with equal probability, and that the steeper post-perihelion index of 3I cannot be regarded as unusual (P. Lacerda et al. 2025).

Finally, we briefly comment on the scattering phase function of 3I. Thanks to the smooth decline in activity and a range of phase angles extending from almost $\sim 30°$ all the way to near-opposition ($\alpha \approx 0°$), we were able not only to robustly constrain the linear part of the phase function, but also its opposition surge, neither of which had been previously measured for 3I. The linear portion of the scattering phase function of 3I appears indistinguishable from those of solar system comets. In contrast, to date there remains a persistent dearth of intensity measurements for cometary dust near zero phase angle (V. Rosenbush et al. 2002). Among the few comets that have been studied in this regime, none have exhibited a distinct opposition effect K. J. Meech & D. C. Jewitt (1987). This phenomenon, however, is widely observed among asteroids, planetary rings, and miscellaneous other airless bodies in the solar system (V. Rosenbush et al. 2002). While we acknowledge that the light scattering mechanisms of cometary dust differ from those of airless surfaces, the opposition effect of 3I qualitatively resembles some of the latter. Although K. J. Meech & D. C. Jewitt (1987) found no opposition effect in their selected sample of solar system comets, the brightness enhancement of 3I we observed is broadly in line with their reported upper limit for the opposition surge of $m_{OE} \lesssim 0.2$ mag.

[8] Overlapping satellite observations showed a more rapid brightening towards perihelion (Q. Zhang & K. Battams 2025), but sampled a mixture of gas and dust continuum emission that cannot be meaningfully interpreted; we ignore them here.

While we cannot rule out the possibility from the available data that the dust grains of 3I are inherently strong backscatterers, we suspect that the detectability of this effect might have been significantly enhanced by concurrent contributions from the orbital plane crossing and the projection of the dust tail. Both factors would increase the total effective cross-section of dust within the photometric aperture, for which we did not correct in Equation (5). We leave the disentanglement of these competing factors to future dust-modelling work. Taken together with the peculiar polarimetric properties reported by Z. Gray et al. (2025); S. Choi et al. (2026), our results suggest that while there are commonalities between dust grains of 3I and solar system comets, unusual physical properties exist.

We did not attempt to constrain the nucleus scattering properties of 3I because of the unconstrained rotation lightcurve modulation from our sparse sampling of the HST observations. Although the near opposition observation from Visit 6 may be influenced by an opposition effect of the nucleus, we posit that the adopted linear phase function typical for cometary nuclei in the solar system for the nucleus of 3I possibly remains valid, given our practice with fitting for the scattering properties of its cometary dust.

5. SUMMARY

This paper presents a photometric analysis of our Hubble Space Telescope observations of interstellar object 3I/ATLAS on the outbound leg of its heliocentric trajectory. Our key findings are as follows:

1. Using the nucleus extraction technique, we successfully revealed the nucleus of 3I and measured its optical cross-section (the product of geometric albedo and physical cross-section) to be $C_{\rm n} = 0.22 \pm 0.07$ km^2. Adopting a nominal V-band geometric albedo of 0.04, typical for cometary nuclei in the solar system, we estimate an effective nucleus radius of $R_{\rm n} = 1.3 \pm 0.2$ km. The result is consistent with our independent estimate derived from the reported nongravitational acceleration and production rates of 3I.

2. The nucleus lightcurve exhibits evidence of temporal variations, likely attributable to either the rotation modulation of an aspherical shape or fluctuations in near-nucleus activity, or both. If due to rotation, the observed brightness range implies a nucleus axis ratio of $2:1$ in the plane of the sky. Unfortunately, none of our HST visits monitored a more complete phase of the lightcurve, making this dataset alone likely not useful for constructing a full phase lightcurve. Using the lightcurve trends we constrain the rotation period to be $\gtrsim 1$ hr.

3. Scattered light by dust grains in the coma displayed a statistically significant opposition surge of ~ 0.2 mag, characterised by an e-folding width of $3^\circ \pm 1^\circ$. This brightening possibly contain coincident contributions from the orbital plane crossing and tail projection. While opposition surges have not been widely reported for solar system cometary dust, the observed brightening is broadly consistent with existing upper limits for solar system comets. The linear portion of the phase function, with a slope of $\beta_\alpha = 0.026 \pm 0.006$ mag degree^{-1}, is indistinguishable from those of solar system comets.

4. Our fixed linear radius aperture photometry indicates that the postperihelion activity of 3I declined smoothly and more rapidly than its preperihelion brightening trend, consistent with our finding that the postperihelion coma surface brightness profile was shallower than its preperihelion counterpart. We measured a postperihelion activity index of $n = 4.5 \pm 0.3$. Such asymmetries in brightening and fading rates are common among solar system comets.

5. Based on the discovery statistics of interstellar objects, we estimate a lower limit of $\gtrsim 1$ 3I-sized (nucleus radius ~ 1.3 km) interstellar object within $r_{\rm H} = 4.5$ au at any instant, which is likely a conservative lower bound as inactive interstellar objects of this size would be significantly more difficult to detect. It is likely that comparably bright interstellar objects have passed through the inner solar system in the era of wide-field CCD surveys; we surmise that such objects have been missed.

ACKNOWLEDGMENTS

We thank Alison Vick for her great efforts on scheduling the HST observations to ensure the successful execution of the HST program. This research is based on observations made with the NASA/ESA Hubble Space Telescope obtained from the Space Telescope Science Institute, which is operated by the Association of Universities for Research in Astronomy, Inc., under NASA contract NAS 5–26555. No NASA funding was used for this work. These observations are associated with program GO/DD 18152.

AUTHOR CONTRIBUTIONS

Facilities: HST (UVIS)

Software: `IRAF` (D. Tody 1986), `L.A.Cosmic` (P. G. van Dokkum 2001), `MPFIT` (C. B. Markwardt 2009), `psffit` (Buie's IDL library)

REFERENCES

Chandler, C. O., Bernardinelli, P. H., Jurić, M., et al. 2025, arXiv e-prints, arXiv:2507.13409, doi: 10.48550/arXiv.2507.13409

Choi, S., Ishiguro, M., Takahashi, J., et al. 2026, arXiv e-prints, arXiv:2601.08591. https://arxiv.org/abs/2601.08591

Cloete, R., Loeb, A., & Vereš, P. 2025, arXiv e-prints, arXiv:2509.21408, doi: 10.48550/arXiv.2509.21408

Cochran, A. L., & Schleicher, D. G. 1993, Icarus, 105, 235, doi: 10.1006/icar.1993.1121

Combi, M. R., Mäkinen, T., Bertaux, J.-L., et al. 2025, arXiv e-prints, arXiv:2512.22354, doi: 10.48550/arXiv.2512.22354

Cordiner, M. A., Roth, N. X., Kelley, M. S. P., et al. 2025, ApJL, 991, L43, doi: 10.3847/2041-8213/ae0647

Denneau, L., Siverd, R., Tonry, J., et al. 2025, Minor Planet Electronic Circulars, 2025-N12, doi: 10.48377/MPEC/2025-N12

Do, A., Tucker, M. A., & Tonry, J. 2018, ApJL, 855, L10, doi: 10.3847/2041-8213/aaae67

Eubanks, T. M., Hibberd, A., Bills, B. G., et al. 2025, Research Notes of the American Astronomical Society, 9, 329, doi: 10.3847/2515-5172/ae2915

Feinstein, A. D., Noonan, J. W., & Seligman, D. Z. 2025, ApJL, 991, L2, doi: 10.3847/2041-8213/adfd4d

Forbes, J. C., & Butler, H. 2025, arXiv e-prints, arXiv:2512.18341, doi: 10.48550/arXiv.2512.18341

Gray, Z., Bagnulo, S., Borisov, G., et al. 2025, ApJL, 992, L29, doi: 10.3847/2041-8213/ae0c08

Groussin, O., Attree, N., Brouet, Y., et al. 2019, SSRv, 215, 29, doi: 10.1007/s11214-019-0594-x

Hui, M.-T., Jewitt, D., Yu, L.-L., & Mutchler, M. J. 2022, ApJL, 929, L12, doi: 10.3847/2041-8213/ac626a

Hui, M.-T., & Li, J.-Y. 2018, PASP, 130, 104501, doi: 10.1088/1538-3873/aad538

Hui, M.-T., Ye, Q.-Z., Föhring, D., Hung, D., & Tholen, D. J. 2020, AJ, 160, 92, doi: 10.3847/1538-3881/ab9df8

Hutsemékers, D., Manfroid, J., Jehin, E., et al. 2025, arXiv e-prints, arXiv:2509.26053, doi: 10.48550/arXiv.2509.26053

Jewitt, D. 1991, in Astrophysics and Space Science Library, Vol. 167, IAU Colloquium 116: Comets in the post-Halley era, ed. R. L. Newburn, Jr., M. Neugebauer, & J. Rahe, 19, doi: 10.1007/978-94-011-3378-4_2

Jewitt, D. 2015, AJ, 150, 201, doi: 10.1088/0004-6256/150/6/201

Jewitt, D., Hui, M.-T., Kim, Y., et al. 2020, ApJL, 888, L23, doi: 10.3847/2041-8213/ab621b

Jewitt, D., Hui, M.-T., Mutchler, M., Kim, Y., & Agarwal, J. 2025, ApJL, 990, L2, doi: 10.3847/2041-8213/adf8d8

Jewitt, D., & Luu, J. 2025, ApJL, 994, L3, doi: 10.3847/2041-8213/ae1832

Jewitt, D., Luu, J., Rajagopal, J., et al. 2017, ApJL, 850, L36, doi: 10.3847/2041-8213/aa9b2f

Jewitt, D., & Seligman, D. Z. 2023, ARA&A, 61, 197, doi: 10.1146/annurev-astro-071221-054221

Jewitt, D. C., & Meech, K. J. 1987, ApJ, 317, 992, doi: 10.1086/165347

Jorda, L., Crovisier, J., & Green, D. W. E. 2008, in LPI Contributions, Vol. 1405, Asteroids, Comets, Meteors 2008, ed. LPI Editorial Board, 8046

Knight, M. M., Kokotanekova, R., & Samarasinha, N. H. 2024, in Comets III, ed. K. J. Meech, M. R. Combi, D. Bockelée-Morvan, S. N. Raymodn, & M. E. Zolensky, 361–404, doi: 10.2458/azu_uapress_9780816553631-ch012

Krist, J. E., Hook, R. N., & Stoehr, F. 2011, in Society of Photo-Optical Instrumentation Engineers (SPIE) Conference Series, Vol. 8127, Optical Modeling and Performance Predictions V, ed. M. A. Kahan, 81270J, doi: 10.1117/12.892762

Lacerda, P., Guilbert-Lepoutre, A., Kokotanekova, R., et al. 2025, A&A, 697, A210, doi: 10.1051/0004-6361/202453565

Lamy, P. L., & Toth, I. 1995, A&A, 293, L43

Lamy, P. L., Toth, I., Fernandez, Y. R., & Weaver, H. A. 2004, in Comets II, ed. M. C. Festou, H. U. Keller, & H. A. Weaver, 223

Lamy, P. L., Toth, I., & Weaver, H. A. 1998, A&A, 337, 945

Markwardt, C. B. 2009, in Astronomical Society of the Pacific Conference Series, Vol. 411, Astronomical Data Analysis Software and Systems XVIII, ed. D. A. Bohlender, D. Durand, & P. Dowler, 251, doi: 10.48550/arXiv.0902.2850

Marsden, B. G., Sekanina, Z., & Yeomans, D. K. 1973, AJ, 78, 211, doi: 10.1086/111402

Martinez-Palomera, J., Tuson, A., Hedges, C., et al. 2025, ApJL, 994, L51, doi: 10.3847/2041-8213/ae1f91

Meech, K. J., & Jewitt, D. C. 1987, A&A, 187, 585

Pickles, A. J. 1998, PASP, 110, 863, doi: 10.1086/316197

Rosenbush, V., Kiselev, N., Avramchuk, V., & Mishchenko, M. 2002, Photometric and Polarimetric Opposition Phenomena Exhibited by Solar System Bodies, ed. G. Videen & M. Kocifaj (Dordrecht: Springer Netherlands), 191–224, doi: 10.1007/978-94-010-0628-6_13

Roth, N. X., Cordiner, M. A., Bockelée-Morvan, D., et al. 2025, arXiv e-prints, arXiv:2511.20845, doi: 10.48550/arXiv.2511.20845

Santana-Ros, T., Ivanova, O., Mykhailova, S., et al. 2025, A&A, 702, L3, doi: 10.1051/0004-6361/202556717

Seligman, D. Z., Micheli, M., Farnocchia, D., et al. 2025, ApJL, 989, L36, doi: 10.3847/2041-8213/adf49a

Tan, H., Yan, X., & Li, J.-Y. 2026, arXiv e-prints, arXiv:2601.15443, doi: 10.48550/arXiv.2601.15443

Taylor, A. G., & Seligman, D. Z. 2025, ApJL, 990, L14, doi: 10.3847/2041-8213/adfa28

Tody, D. 1986, in Society of Photo-Optical Instrumentation Engineers (SPIE) Conference Series, Vol. 627, Instrumentation in astronomy VI, ed. D. L. Crawford, 733, doi: 10.1117/12.968154

van Dokkum, P. G. 2001, PASP, 113, 1420, doi: 10.1086/323894

Willmer, C. N. A. 2018, ApJS, 236, 47, doi: 10.3847/1538-4365/aabfdf

Xing, Z., Oset, S., Noonan, J., & Bodewits, D. 2025, ApJL, 991, L50, doi: 10.3847/2041-8213/ae08ab

Yang, B., Meech, K. J., Connelley, M., Zhao, R., & Keane, J. V. 2025, ApJL, 992, L9, doi: 10.3847/2041-8213/ae08a7

Ye, Q., Kelley, M. S. P., Hsieh, H. H., et al. 2025, ApJL, 993, L31, doi: 10.3847/2041-8213/ae147b

Zhang, Q., & Battams, K. 2025, arXiv e-prints, arXiv:2510.25035, doi: 10.48550/arXiv.2510.25035